Endogenous retroviruses are associated with hippocampus-based memory impairment

Roman Sankowski[a,b,c,d,e], Joshua J. Strohl[b,f,g], Tomás S. Huerta[b,f,g], Elham Nasiri[a,b], Andrea N. Mazzarello[h], Cristina D'Abramo[i], Kai Fan Cheng[a], Ori Staszewski[d,e], Marco Prinz[d,j,k], Patricio T. Huerta[b,f,g,1,2], and Yousef Al-Abed[a,f,g,1,2]

[a]Center for Molecular Innovation, Feinstein Institutes for Medical Research, Manhasset, NY 11030; [b]Laboratory of Immune & Neural Networks, Feinstein Institutes for Medical Research, Manhasset, NY 11030; [c]Elmezzi Graduate Program, Feinstein Institutes for Medical Research, Manhasset, NY 11030; [d]Institute of Neuropathology, Faculty of Medicine, University of Freiburg, 79085 Freiburg, Germany; [e]Berta-Ottenstein Programme for Clinician Scientists, Faculty of Medicine, University of Freiburg, 79085 Freiburg, Germany; [f]Department of Molecular Medicine, Zucker School of Medicine at Hofstra/Northwell, Hempstead, NY 11549; [g]Institute of Bioelectronic Medicine, Feinstein Institutes for Medical Research, Manhasset, NY 11030; [h]Karches Center for Oncology Research, Feinstein Institutes for Medical Research, Manhasset, NY 11030; [i]Litwin-Zucker Center for Alzheimer's Disease & Memory Disorders, Feinstein Institutes for Medical Research, Manhasset, NY 11030; [j]Signalling Research Centres, Centre for Biological Signalling Studies (BIOSS) and Centre for Integrative Biological Signalling Studies (CIBSS), University of Freiburg, 79085 Freiburg, Germany; and [k]Center for Basics in NeuroModulation (NeuroModulBasics), Faculty of Medicine, University of Freiburg, 79085 Freiburg, Germany

Edited by Lawrence Steinman, Stanford University School of Medicine, Stanford, CA, and approved October 21, 2019 (received for review January 29, 2019)

Retrotransposons compose a staggering 40% of the mammalian genome. Among them, endogenous retroviruses (ERV) represent sequences that closely resemble the proviruses created from exogenous retroviral infection. ERVs make up 8 to 10% of human and mouse genomes and range from evolutionarily ancient sequences to recent acquisitions. Studies in *Drosophila* have provided a causal link between genomic retroviral elements and cognitive decline; however, in mammals, the role of ERVs in learning and memory remains unclear. Here we studied 2 independent murine models for ERV activation: muMT strain (lacking B cells and antibody production) and intracerebroventricular injection of streptozotocin (ICVI-STZ). We conducted behavioral assessments (contextual fear memory and spatial learning), as well as gene and protein analysis (RNA sequencing, PCR, immunohistochemistry, and western blot assays). Mice lacking mitochondrial antiviral-signaling protein (MAVS) and mice lacking stimulator of IFN genes protein (STING), 2 downstream sensors of ERV activation, provided confirmation of ERV impact. We found that muMT mice and ICVI-STZ mice induced hippocampal ERV activation, as shown by increased gene and protein expression of the Gag sequence of the transposable element intracisternal A-particle. ERV activation was accompanied by significant hippocampus-related memory impairment in both models. Notably, the deficiency of the MAVS pathway was protective against ICVI-STZ–induced cognitive pathology. Overall, our results demonstrate that ERV activation is associated with cognitive impairment in mice. Moreover, they provide a molecular target for strategies aimed at attenuating retroviral element sensing, via MAVS, to treat dementia and neuropsychiatric disorders.

endogenous retrovirus | hippocampus | cognitive impairment | learning and memory | inflammation

While genomic stability ensures the survival of a species, a certain degree of genomic instability is essential for evolutionary success in changing environments. Retrotransposons constitute approximately 40% of the mammalian genome and are major drivers for genomic evolution (1–3). Three major classes of retrotransposons are found in the mammalian genome: long interspersed nuclear elements (LINEs; ∼17% of the sequenced genome), short interspersed nuclear elements (SINEs; ∼10%) and long terminal repeat retrotransposons (LTRs; ∼8 to 10%) (1, 2). The latter class is also known as endogenous retroviruses (ERVs), as they contain a retroviral structure with 1 or more genes for *gag*, *pol*, *pro*, and *env* flanked by LTRs that serve as promoters (4, 5). In humans, 0.1% of spontaneous mutations are due to retrotransposon insertion and ∼95% of these are caused by SINE or LINE activities (6, 7).

Strikingly, ∼10 to 15% of spontaneous mutations in mice are caused by ERV insertions, most of which are due to intracisternal A-particles (IAPs) (7). IAPs are present at ∼1,000 copies throughout the mouse genome, showing high retrotransposon activity (8, 9). IAPs are devoid of infectivity due to loss of the *env* gene (10). In addition to their evolutionary role, it is tempting to consider the role of retrotransposons in somatic cells, particularly in organisms past reproductive age, as aging has been shown to facilitate genomic instability (11).

To control the autonomous activity of retrotransposons, mammals have evolved molecular mechanisms that broadly overlap with antiviral immune defense (12). These mechanisms include DNA methylation (13–16), nucleic acid sensing Toll-like receptors (TLRs) (17), cytosolic and lysosomal DNases (18, 19), immunoglobulins (20, 21), and others (12). Disruption of these mechanisms leads to derepression of retrotransposons, with subsequent

Significance

Endogenous retroviruses (ERVs) consist of interspersed genomic elements derived from retroviral infections that invaded our ancestral germ lines. Notably, ERVs compose 8 to 10% of the human and mouse genomes. Until recently, ERVs were considered unimportant, so-called "junk" DNA. However, this naïve characterization has changed dramatically as distinct ERV-related functions are revealed in heath and disease. In this study, we demonstrate that chronic ERV activation is associated with cognitive impairment, measured with hippocampus-related tasks, in a mouse model. We confirm these findings in an independent mouse model of acute retroviral activation and show that cognitive deficits are mitigated in the absence of the retroviral RNA sensor protein MAVS. Our results point to an underappreciated therapeutic modality for impaired cognition.

Author contributions: R.S., J.J.S., T.S.H., O.S., M.P., P.T.H., and Y.A.-A. designed research; R.S., J.J.S., T.S.H., E.N., A.N.M., C.D., K.F.C., O.S., and P.T.H. performed research; R.S., A.N.M., M.P., and Y.A.-A. contributed new reagents/analytic tools; R.S., J.J.S., T.S.H., E.N., C.D., K.F.C., O.S., and P.T.H. analyzed data; and R.S., P.T.H., and Y.A.-A. wrote the paper.

The authors declare no competing interest.

This article is a PNAS Direct Submission.

Data deposition: The data reported in this paper have been deposited in the Gene Expression Omnibus (accession no. GSE137782). The R code used to prepare figures is provided at https://github.com/rsankowski/sankowski-et-al-pnas-2019/.

[1]P.T.H. and Y.A.-A. contributed equally to this work.

[2]To whom correspondence may be addressed. Email: phuerta@northwell.edu or yalabed@northwell.edu.

This article contains supporting information online at https://www.pnas.org/lookup/suppl/doi:10.1073/pnas.1822164116/-/DCSupplemental.

First published December 2, 2019.

morbidity and mortality through autoimmunity and malignancy (13, 14, 17–21). Along with aberrant retrotransposon activation, the underlying pathogenic mechanisms include antiviral immunity by ERV RNAs that activate nucleic acid sensors, such as TLRs, mitochondrial antiviral signaling protein (MAVS), and stimulator of IFN genes protein (STING) (19, 22, 23). Acquisition and transmission of infectious ERVs has been reported in high-leukemic laboratory mouse strains (24) as well as in wild mice (25). Interestingly, the spontaneous emergence of ecotropic leukemia virus has been shown under conditions of ERV derepression and aging in low-leukemic mouse strains (17, 20, 21, 26). Moreover, diabetic rodents display spontaneous and chemically induced emergence of IAP (27–29). Given this evidence for ERVs as drivers of pathology, we sought to investigate whether ERV derepression might affect brain function.

ERV expression transcripts, and even retroviral proteins, have been found in the brain of mice and humans (30, 31). Mutations associated with retrotransposon activation have been implicated in hereditary human neurodegenerative syndromes and autoimmune disorders (18, 32–34). ERV accrual has also been described in sporadic brain diseases; for instance, human endogenous retrovirus K (HERV-K) is elevated in patients with amyotrophic lateral sclerosis (33–36), HERV-W is high in multiple sclerosis (37, 38), and LTR and non-LTR retrotransposons are elevated in Alzheimer's disease (AD) (39). Strikingly, an emergent encephalitic ERV found in wild mice recapitulates aspects of amyotrophic lateral sclerosis (25). An elegant *Drosophila* study has described causal links among aging-induced retrotransposon activation, neurodegeneration, and learning impairment (40). Taken together, these studies suggest that ERV activation constitutes a plausible mechanistic link among aging, inflammation, and neurodegeneration.

The role of ERVs in mouse behavior remains largely unexplored. Here we investigate hippocampus-based cognition in 2 independent murine models of ERV activation. The first model is the muMT strain, which consists of a genetic knockout (KO) of the Ig heavy constant mu gene, leading to defective B cell maturation and well-described peripheral ERV induction (21). The second model is chemically induced by STZ, a diabetogenic carbohydrate compound (27, 28), which we applied via intracerebroventricular injection (ICVI-STZ). ICVI-STZ has been used as a model for sporadic AD (41). Our data reveal a clear up-regulation of ERV transcripts in both models along with gliosis, proinflammatory cytokine expression, and structural changes of hippocampal pyramidal neurons in muMT mice. Notably, both models show pronounced disruptions of contextual fear memory (CFM) and spatial learning. The cognitive impairments are attenuated in a KO strain lacking the cytosolic viral RNA sensor protein MAVS. Our data point toward ERV activation as an endogenous contributor to brain inflammation and cognitive dysfunction, and support exploration of the MAVS pathway in therapeutic drug discovery efforts.

Results

muMT Mice Show Hippocampal ERV Activation and Cognitive Impairment. Spontaneous emergence of an ecotropic murine leukemia virus (eMLV) was recently described in antibody-deficient muMT mice (21), but data on brain inflammation and cognition are scanty in this strain (42). Western blot and immunohistochemistry analyses of hippocampi from adult muMT mice showed marked up-regulation of the astrocytic marker glial fibrillary acidic protein (GFAP) and increased astrocytic cell densities compared with WT controls (Fig. 1 *A* and *B*). The microglial marker ionized calcium-binding adapter molecule 1 (IBA1; encoded by the *Aif1* gene) and microglia cell density were unchanged (Fig. 1 *A* and *B*). In addition, we found up-regulation of the p35 cleavage product of the IAP Gag polyprotein, indicating IAP activation (Fig. 1*A*). Transcriptome analysis of hippocampal lysates using RNA-seq returned 365 differentially up-regulated genes in muMT mice ($n = 2$) and 682 in WT mice ($n = 3$) (Fig. 1*C*). Interestingly, muMT mice showed up-regulation of MHC I and MHC II genes (e.g., *B2m* and *H2-K1*), oligodendrocyte-enriched genes (e.g., *Mog* and *Mag*), and the *Psenen* gene that encodes presenilin-enhancer 2, a subunit of the protein γ-secretase (Fig. 1*C*). WT mice showed up-regulation of synaptic genes (e.g., *Homer2*), histone modification-associated genes (e.g., *Kdm5c*), genes associated with insulin signaling (e.g., *Ide* and *Ptprn2*), and transmembrane transporters (e.g., *Kcna1* and *Slc4a10*) (Fig. 1*C*).

Functional Gene Ontology (GO) showed enrichment of such terms as "synapse organization" for WT mice and "gliogenesis" and "response to unfolded protein" for muMT mice (Fig. 1*D*). Up-regulation of unfolded protein response as a form of endoplasmic reticulum (ER) stress may be due to IAP accumulation in the ER (8). Furthermore, changes in genes associated with myelination may reflect the involvement of B cells in oligodendrocyte biology (43). Mapping of the RNA-seq data to a reference genome containing retrotransposons revealed 30 differentially expressed genes in muMT mice and 27 genes in WT mice (Fig. 1*E*). Notably, muMT mice showed higher levels of ERVK, the ERV family that includes IAP (5 elements in muMT vs. 2 elements in WT), and also L1 (8 elements in muMT vs. 2 elements in WT) (Fig. 1*F*). The levels for the other retrotransposons were comparable in the muMT and WT groups. Validation analysis using PCR confirmed robust up-regulation of IAP LTR, IAP Gag, IAPEz-Int, and eMLV in the muMT group (Fig. 1*G*). Furthermore, muMT mice showed significant up-regulation of *Irf5*, *Irf7*, and *Ilb* (Fig. 1*G*).

Behavioral assessment revealed that the muMT mice were hyperactive in the open field task, with increased distance moved (Fig. 1*H*) and time spent in the central quadrant (*SI Appendix*, Fig. S1*A*). The muMT mice also showed decreased motor coordination in the rotarod test (*SI Appendix*, Fig. S1*B*). Interestingly, hyperactivity has been associated with cognitive deficits in AD mouse models (44, 45). Remarkably, muMT mice were significantly impaired in the test for CFM (Fig. 1*I*) and the clockmaze test for spatial learning (*SI Appendix*, Fig. S1 *C* and *D*). Morphological studies of pyramidal neurons in the dorsal hippocampus of muMT mice using Golgi staining combined with Sholl analysis showed no changes in apical dendrites and marked reduction in the complexity of basal dendrites (Fig. 1*J*). Spine densities were comparable in the 2 strains (Fig. 1*K*). Immunohistochemistry in the hippocampus with markers for neurons (NeuN), astrocytes (GFAP), microglia (IBA1), and T cells (CD3), each combined with IAP Gag antiserum, showed immunopositivity of IAP Gag in neurons and microglia but not in astrocytes or T cells (Fig. 2*A*). In WT mice, IAP Gag was observed in neurons but not in microglia (Fig. 2*B*).

Next, considering the disruption of B cell biology in muMT mice, we asked whether altering other immune cells could affect ERV expression. For this purpose, we examined NOD-Scid-γ (NSG) mice (lacking B cells, T cells, and natural killer cells), with nonobese diabetic (NOD) mice serving as controls. Hippocampal protein lysates from NSG mice showed increased GFAP immunoreactivity compared with control NOD mice (*SI Appendix*, Fig. S2*A*). In line with muMT mice and previous reports (16), eMLV was up-regulated in NSG mice, while IAP was unchanged (*SI Appendix*, Fig. S2*A*). Likewise, there were no alterations in the levels of IBA1, IAP Gag protein, and the expression levels of LINE, SINE, *Gfap*, *Aif1*, *Ifna*, *Il12a*, and *Il6* (*SI Appendix*, Fig. S2*A*). Cognitive testing was not conducted in NSG mice owing to known cognitive deficits in T cell-deficient mice (46).

Taken together, our data reveal that antibody-deficient mice showed hippocampal expression of eMLV and IAP with increased GFAP protein levels, decreased expression levels of genes associated with synaptic organization and transmembrane solute transport in the RNA-seq, reduced complexity of hippocampal pyramidal neurons, hyperactivity, impaired contextual memory, and spatial learning deficit.

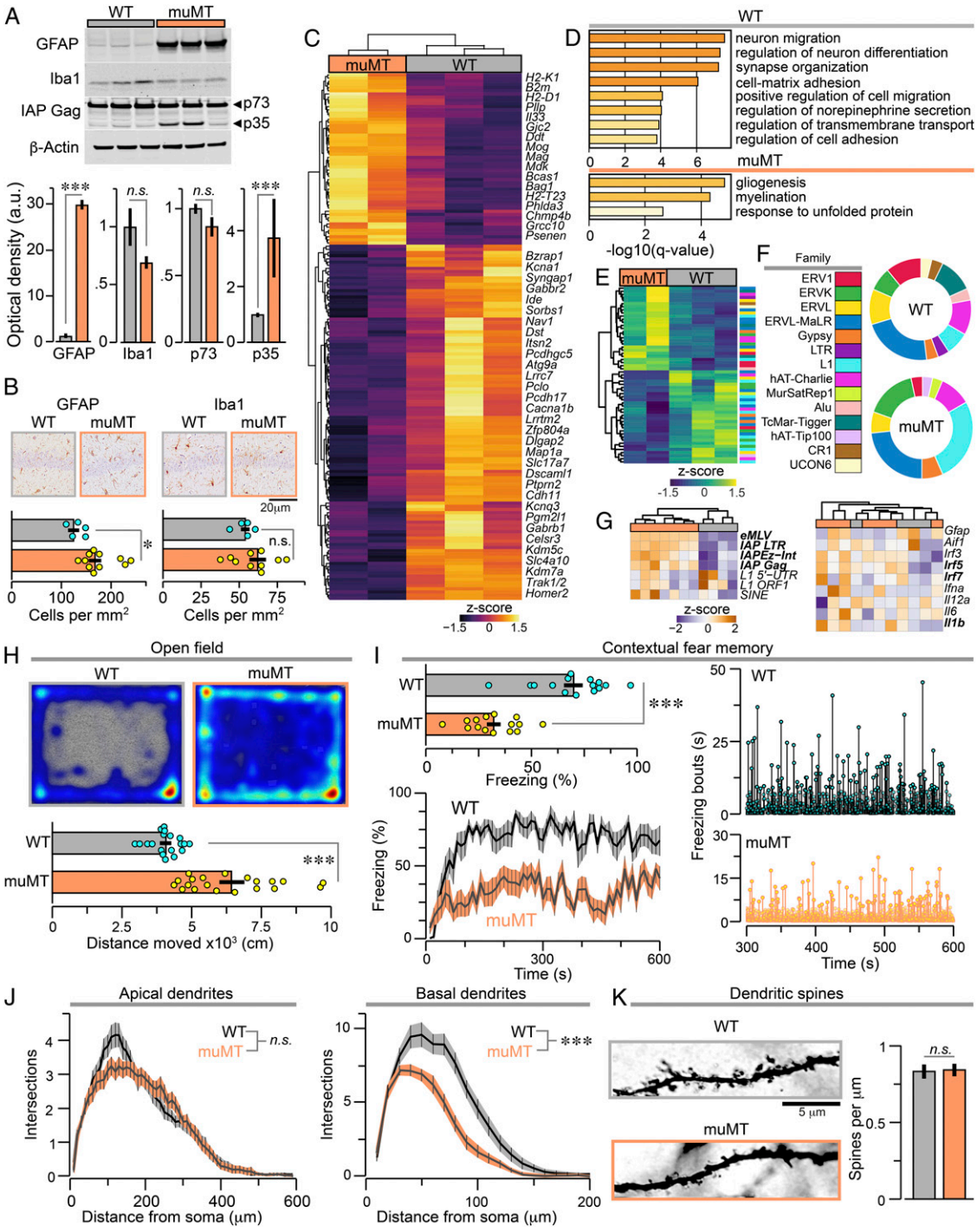

Fig. 1. Cognitive deficit and robust ERV activation in the hippocampus of muMT mice. (*A*–*G*) Hippocampal protein and gene expression in muMT and WT mice. (*A*) Western blots from protein lysates and densitometry of GFAP ($n = 3$ per group), IBA1 ($n = 3$ per group), and IAP Gag polyprotein ($n = 9$ muMT; $n = 8$ WT). ***$P < 0.001$, 1-sided Mann–Whitney *U* (MWU) test. (*B*) Immunohistochemical cell density analysis of GFAP- and IBA1-positive cells ($n = 10$ muMT; $n = 5$ WT). *$P < 0.05$, MWU test; each dot represents a mouse. (*C*) Heatmap of differentially expressed genes obtained from RNA-seq ($n = 2$ muMT, 365 genes; $n = 3$ WT, 682 genes). Selected gene names are displayed next to the heatmap. (*D*) Selected enriched GO terms based on differentially expressed genes from *C*. (*E*) Heatmap showing differentially expressed transposable elements (muMT, 30 genes; WT, 27 genes). (*F*) Donut plots depicting the composition of differentially expressed transposable elements, color-coded for the respective families. (*G*) Heatmaps of the qPCR data for selected retrotransposons (*Left*) and inflammation-related (*Right*) genes. Each cell represents 1 animal. Genes printed in bold show statistical significance at $P < 0.05$. The hierarchical clustering of samples indicates differences between them. Note that muMT and WT mice cluster separately with respect to retrotransposons but not to inflammation-related genes. (*H*) Open field test with representative heatmaps and mean distance moved ($n = 20$ mice per group). ***$P < 0.001$, MWU test; 1 dot per mouse. (*I*) Freezing response. (*Top Left*) Bar graphs of the freezing response during the last 5 min of the CFM test ($n = 15$ mice per group). ***$P < 0.001$, MWU test, 1 dot per mouse. (*Bottom Left*) Freezing across the trial (mean ± SEM). (*Right*) Lollipop plots depicting the duration of individual freezing bouts; note the different heights of the *y*-axes with same scale. (*J*) Sholl analysis of apical and basal dendrites of hippocampal pyramidal cells ($n = 3$ mice per group). ***$P <$ 0.001, mixed-effects model. (*K*) Representative microscope images of dendritic spines and comparison of spine density in WT and muMT mice. The bar graphs in *A*, *B*, *H*, *I*, and *K* represent mean ± SEM. *n.s.*, *P* not significant.

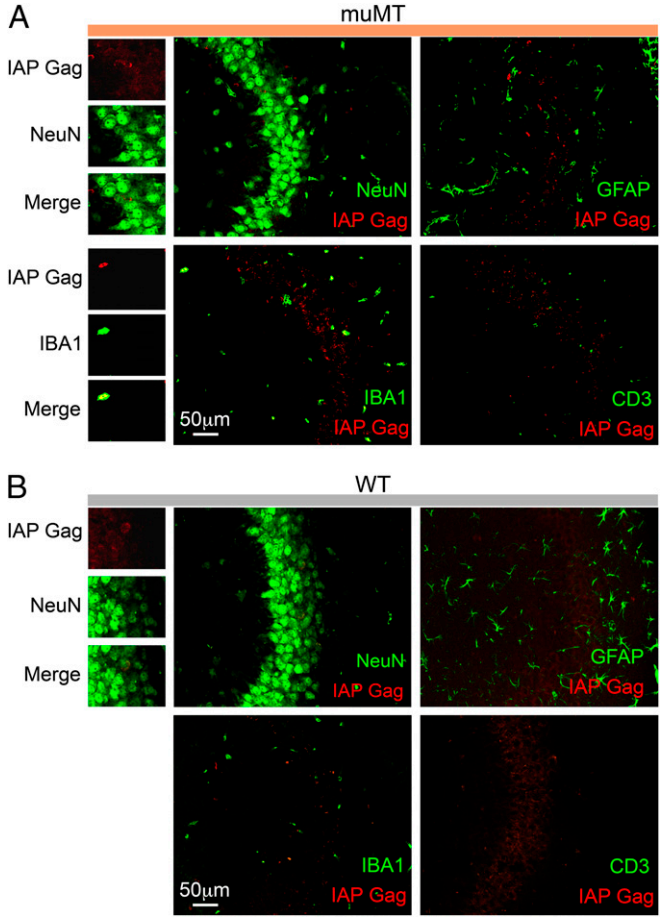

Fig. 2. Western blot and coimmunohistochemistry analyses of IAP Gag. (*A*) Coimmunohistochemistry of IAP Gag protein with markers for neurons (NeuN), microglia (IBA1), astrocytes (GFAP), and T cells (CD3) in muMT mice ($n = 3$). (*B*) Coimmunohistochemistry of IAP Gag in WT mice ($n = 3$).

ICVI-STZ Induces Hippocampal ERV Activation and Cognitive Impairment. To generate ICVI-STZ mice, we injected 6-mo-old male C57BL/6 mice with STZ (3 mg/kg) in the left ventricle. Vehicle injection (ICVI-Veh) served as a control. After 14 d, analysis of hippocampal protein expression revealed that ICVI-STZ mice had elevated immunoreactivity for GFAP, IBA1, and the IAP Gag polyprotein products p73 and p35 (Fig. 3*A*). Interestingly, the gross morphology of the hippocampus remained unchanged following STZ injection (*SI Appendix*, Fig. S3*A*). IAP Gag diffusely colocalized with hippocampal neurons (*SI Appendix*, Fig. S3*D*). Immunohistochemical analysis revealed increased astrocyte density in hippocampi of ICVI-STZ mice (Fig. 3*B*). RNA-seq analysis returned 29 differentially expressed genes in ICVI-STZ mice ($n = 3$) and 372 genes in ICVI-Veh mice ($n = 2$) (Fig. 3*C*). Furthermore, the ICVI-STZ group showed an antiviral gene signature with up-regulation of *Irf7* and *Ifit3* and enrichment of the GO term "response to virus" (Fig. 3 *C* and *D*). ICVI-Veh mice showed up-regulation of several transmembrane solute carriers, metabolism-associated genes such as *Lepr* (leptin receptor) and *Igfr2* (insulin-like growth factor 2), and synaptic genes involved in histone modifications, such as *Kat2b* and *Dydc2* (Fig. 3*C*). GO terms enriched in ICVI-Veh mice included "import across plasma membrane" and "production of TGF-β" (Fig. 3*D*). Notably, disruption of insulin signaling has been previously shown in ICVI-STZ mice and 3xTg-AD mice (47). Furthermore, we found up-regulation of retrotransposons of the ERVK family (3 elements in ICVI-STZ vs. none in ICVI-Veh, including the gene IAPLTR4) and the ERVL family (1 element in ICVI-STZ vs. none in ICVI-Veh) (Fig. 3 *E* and *F*). PCR assays confirmed the up-regulation of IAP as well as transcripts mapping to eMLV and SINE and also confirmed up-regulation of *Irf7*, *Irf5*, *Aif1*, *Il1b*, and *Il6* (Fig. 3*G*).

ERV activation was previously reported in aged C57BL/6 mice (26). We used PCR to assess gene expression in 30-mo-old C57BL/6 mice ($n = 6$) with respect to 6-mo-old C57BL/6 controls ($n = 4$) aged in the same animal facility. The 30-mo-old mice showed marked up-regulation of GFAP, while IBA1 was unchanged (*SI Appendix*, Fig. S2*B*). Significantly increased gene expression was found for eMLV, *Gfap*, and *Ifna*, whereas expression levels of IAP, LINE, and SINE remained unchanged (*SI Appendix*, Fig. S2*B*). Thus, IAP activation appeared to be specific to ICVI-STZ mice and was not spontaneously induced in very old mice.

Behavioral testing performed 3 to 6 wk after injection in ICVI-STZ mice showed no changes in the open field task (Fig. 3*H* and *SI Appendix*, Fig. S3*B*) but strikingly impaired CFM (Fig. 3*I*). Furthermore, ICVI-STZ mice showed spatial learning deficit in the clockmaze test (*SI Appendix*, Fig. S3*C*). Sholl analysis of dorsal hippocampal pyramidal neurons showed no changes in apical and basal dendrites (Fig. 3*J*), but dendritic spine density was significantly reduced (Fig. 3*K*). Thus, ICVI-STZ induced hippocampal IAP, an antiviral immune response, cognitive deficits, and reduced dendritic spine density. In addition, ICVI-STZ induced gene expression changes in metabolic and membrane channel genes.

STZ-Induced Activation of IAP in Primary Brain Cells. The strong up-regulation of GFAP observed in muMT (Fig. 1*A*), NSG (*SI Appendix*, Fig. S2*A*), and ICVI-STZ (Fig. 3*A*) mice prompted us to further examine the effect of STZ on primary astrocyte cultures. Cytotoxicity studies in primary murine astrocytes showed lactate dehydrogenase (LDH) secretion after 48 h of treatment with STZ at concentrations of ≥4 mM (Fig. 4*A*). Our calculations showed that in vivo concentrations of STZ reach up to 2 mM. To avoid confounding effects of cell death, we treated primary astrocytes for 48 h with STZ, which produced a dose-dependent up-regulation of IAP LTR, Ez-INT, and *Gag* expression (Fig. 4*B*). Genomic DNA (gDNA) methylation has been identified as a major mechanism of IAP suppression (12–14, 16). Thus, to further understand the mechanisms underlying STZ-induced IAP up-regulation, we considered the possibility that STZ treatment might be interfering with gDNA methylation (48). Targeted bisulfite sequencing of the IAP *Gag* gene in astrocytes showed no changes in methylation after a 48-h treatment with 2-mM STZ (Fig. 4 *C* and *D*). Thus, noncytotoxic concentrations of STZ were capable of activating IAP in primary astrocytes, independent of gDNA methylation.

MAVS Deficiency Provides Resistance to ICVI-STZ–Induced Cognitive Impairment. Cytosolic nucleic sensors provide a main line of defense against cytosolic retroviral RNA accrual (15, 22, 23). MAVS and STING proteins are adapters of cytosolic sensors of viral RNA and DNA, respectively (49, 50). We reasoned that if ICVI-STZ–induced cognitive deficits were driven by an inflammatory response to ERV activation, then MAVS and/or STING deficiency might be protective. We thus tested this hypothesis with a genetic engineering approach using a KO strain lacking MAVS (MAVS-KO) or STING (STING-KO).

MAVS-KO mice were injected with ICVI-STZ or ICVI-Veh, and hippocampal morphology, hippocampal gene expression, and hippocampus-based behavioral tests were conducted. MAVS-WT mice of the same strain served as controls. Immunohistochemical analysis showed increased astrocyte cell density in ICVI-STZ–injected MAVS-WT mice but not in the MAVS-KO mice (Fig. 5 *A* and *B*). However, MAVS-KO mice showed increased astrocyte density at baseline (Fig. 5*B*). RNA-seq analysis of MAVS-KO

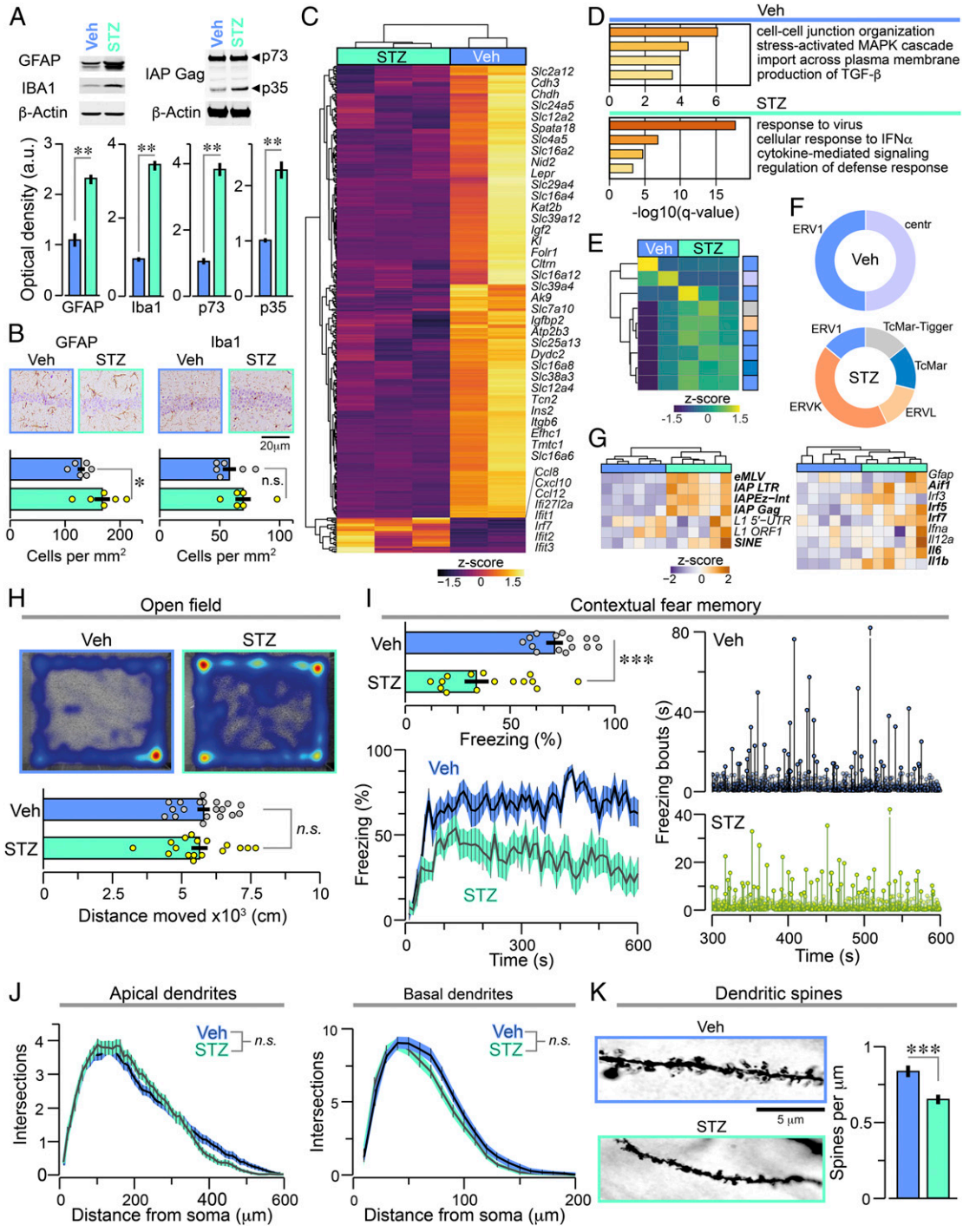

Fig. 3. ICVI-STZ WT mice display hippocampal ERV activation, inflammation, and cognitive deficit. (*A*–*G*) Hippocampal protein and gene expression in ICVI-STZ and ICVI-Veh mice. (*A*) Western blots of hippocampal protein lysates obtained from ICVI-Veh or ICVI-STZ mice with densitometry of GFAP ($n = 4$ per group), IBA1 ($n = 4$ per group), and IAP Gag polyprotein ($n = 7$ ICVI-STZ; $n = 6$ ICVI-Veh). $^{**}P < 0.01$, MWU test. (*B*) Immunohistochemical cell density analysis of GFAP+ and IBA1+ cells ($n = 5$ per group). $^{*}P < 0.05$, MWU test; 1 dot per mouse. (*C*) Heatmap of differentially expressed genes obtained from RNA-seq analysis ($n = 3$ ICVI-STZ, 29 genes; $n = 2$ ICVI-Veh, 372 genes). Selected genes are displayed next to the heatmap. (*D*) Selected enriched GO terms based on the differentially expressed genes from *C*. (*E*) Heatmap showing differentially expressed transposable elements (ICVI-STZ, 7 genes; ICVI-Veh, 2 genes). (*F*) Donut plots depicting the composition of differentially expressed transposable elements, color-coded for the respective families. (*G*) Heatmaps of the qPCR results for selected retrotransposons (*Left*) and inflammation-related genes (*Right*). Each cell represents 1 animal. Genes printed in bold type show statistical significance at $P < 0.05$. Note that hierarchical clustering separated ICVI-STZ and ICVI-Veh mice with respect to retrotransposons and inflammation-related genes. (*H* and *I*) Behavioral assessment ICVI mice at 3 wk after intracerebroventricular injection. (*H*) Open field test: representative heatmaps and distance moved ($n = 17$ ICVI-STZ; $n = 19$ ICVI-Veh; 1 dot per mouse). (*I*) Fear conditioning. (*Top Left*) Bar graphs of the freezing response ($n = 15$ mice per group) $^{***}P < 0.001$, MWU test; 1 dot per mouse. (*Bottom Left*) Freezing across the trial (mean ± SEM). (*Right*) Lollipop plots depicting durations of freezing bouts. Note the different heights of the *y*-axes with the same scale. (*J* and *K*) Hippocampal neural morphology of ICVI-STZ and ICVI-Veh mice. (*J*) Sholl analysis of apical and basal dendrites ($n = 3$ mice per group). (*K*) Spine density analysis with representative images of dendritic spines and comparison of spine densities between ICVI-STZ and ICVI-Veh mice ($n = 3$ mice per group). $^{***}P < 0.001$, MWU test. The bar graphs in *A*, *B*, *H*, *I* and *K* represent mean ± SEM. *n.s.*, *P* not significant.

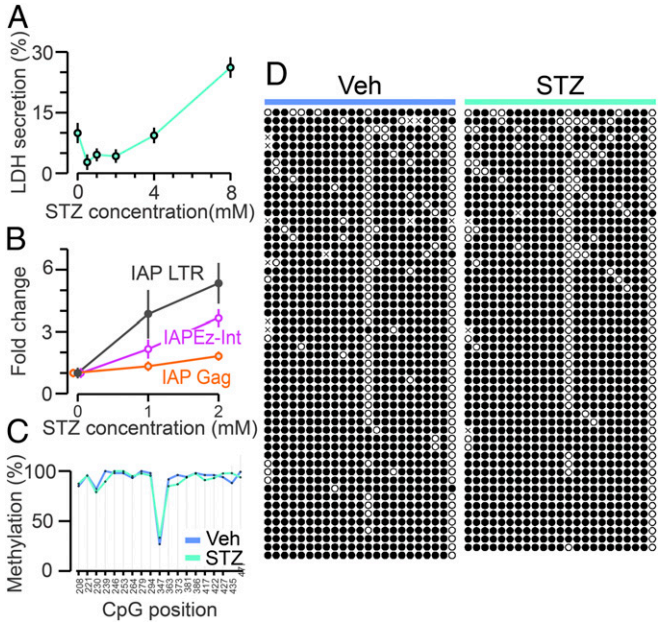

Fig. 4. In vitro studies in primary astrocytes. (*A*) Dose-dependent LDH secretion of primary astrocytes in response to STZ. (*B*) qPCR analysis of the expression of IAP LTR, IAPEz-Int, and IAP Gag after 48 h of STZ treatment. (*C* and *D*) Targeted bisulfite sequencing of the IAP Gag gene in primary astrocytes. (*C*) Quantification of the percentage of methylation at CpG methylation sites. (*D*) Visualization of methylation across CpGs. (Veh: $n = 54$ clones sequenced; STZ: $n = 53$ clones sequenced; filled circle, methylated CpG; empty circle, unmethylated CpG; x, nonconsensus).

mice returned 94 differentially expressed genes in the ICVI-STZ group ($n = 3$) and 90 genes in the ICVI-Veh group ($n = 4$) (Fig. 5*C*). MAVS-KO-ICVI-STZ mice showed up-regulation of MHC II genes (e.g., *H2-T24*), histone modification genes (e.g., *Kdm7a*), and genes involved in insulin signaling (e.g., *Irs4*) (Fig. 5*C*). The corresponding enriched GO terms included "regulation of cell response to stress" and "response to unfolded protein response" (Fig. 5*D*). MAVS-KO-ICVI-Veh mice displayed up-regulation of synapse-associated genes (e.g., *Filip1*), insulin-signaling genes (e.g., *Igfbp4*), and cell membrane transporters (e.g., *Kcna4*), as well as GO terms including "circadian behavior" (Fig. 5 *C* and *D*). Retrotransposon-based RNA-seq analysis showed broad changes between ICVI-STZ ($n = 20$ genes) and ICVI-Veh ($n = 64$ genes) (Fig. 5*E*). Interestingly, the ratio of ERVK remained constant after ICVI-STZ (Fig. 5*E*). Major changes were up-regulation of the Alu SINE family (8 elements in ICVI-STZ vs. none in ICVI-Veh) and down-regulation of the L1 LINE family (2 elements in ICVI-STZ vs. 27 elements in ICVI-Veh) (Fig. 5*E*). Confirmation using PCR showed a normal response to ICVI-STZ in MAVS-WT mice, with up-regulation of IAP, SINE, and L1 as well as *Il1b*, *Irf3*, *Irf5*, and *Irf7* (Fig. 5*F*). In contrast, MAVS-KO responded to ICVI-STZ with changes in L1 and *Ifna* expression (Fig. 5*G*). Opposite changes in L1 expression between PCR and RNA-Seq could potentially be observed in biases introduced through the PCR primer design or reduced sensitivity of RNA-Seq. Cognitive testing showed that MAVS-KO mice were resistant to ICVI-STZ–induced disruptions of CFM in the fear conditioning paradigm (Fig. 5*H*). Testing for spatial learning in the clock-maze paradigm was inconclusive (*SI Appendix*, Fig. S4 *A* and *B*). Thus, MAVS-KO mice displayed attenuated ERV activation, lack of associated antiviral immune response, and rescue of hippocampal learning deficits. ICVI-STZ induced the induction of unfolded protein response, histone-modifying, and cell membrane transporter genes.

To further understand the effect of ERVs in the ICVI-STZ model, we injected STING-KO mice, which are deficient in the DNA-sensor STING (49). Immunohistochemistry of STING-KO brains revealed pronounced astrogliosis and loss of hippocampal neurons adjacent to the left ventricle following ICVI-STZ injection (Fig. 6*A*). PCR analysis revealed up-regulation of IAP LTR, IAPEz-Int, and L1 ORF1 as well as *Gfap*, *Aif1*, *Il6*, and *Il1b* (Fig. 6*B*). Unexpectedly, STING-KO mice failed to show learning in the fear conditioning test and clockmaze paradigms at baseline (*SI Appendix*, Fig. S4*D*). These data show that STING-KO mice displayed exacerbation of ICVI-STZ–induced pathology, including ERV activation along with pronounced hippocampal neuron loss and gliosis.

Discussion

The present study shows that ERV activation is associated with hippocampus-related learning deficits in mice and suggests that these effects are mediated by the cytosolic RNA sensor MAVS. Earlier evidence showed leukemia, autoimmunity and meningoencephalitis with motor neuron pathology associated with ERV activation (13, 14, 17–21, 25, 33). Using 2 independent mouse models, muMT and ICVI-STZ mice, we have shown that hippocampus-based learning is disrupted in mice with ERV activation. Acute ERV activation in ICVI-STZ mice induces a robust antiviral immune response mediated through *Irf7*, which seems to be attenuated in muMT mice with chronic ERV activation. Notably, muMT mice show down-regulation of several genes involved in synaptic function and mimic behavioral aspects found in AD mouse models (44, 45).

While the muMT and the ICVI-STZ models have different modes of ERV activation, we find several commonalities. Both models show up-regulation of immune response genes and down-regulation of genes involved in histone modifications, insulin signaling, and transmembrane transport. Immune activation can be explained by the immunogenic activity of ERVs. Moreover, disruptions of insulin signaling have been found in AD mouse models (47) and human AD (51). Transmembrane transporter disruptions may be explained in light of impaired neuronal connectivity (52). Histone modification changes may be seen in the context of ERV repression (12–16). Genomic insertion is an important aspect of the retrotransposon life cycle and somatic mutagenesis (13, 14, 17, 20). The massive gliosis and neuronal loss seen in the STING-KO-ICVI-STZ mice may be driven by pronounced DNA damage through retrotransposons. Thus, STING may serve as a barrier against retrotranscribed insertion-competent ERV-DNA.

A limitation of our study is that due to the genomic abundance of ERVs, causal proof is challenging, as elimination of all ERVs is not feasible. Nonetheless, we show that deficiency of the intracellular RNA sensor adapter MAVS rendered mice resistant to ICVI-STZ–induced cognitive deficits.

The finding that ERV activation appeared to be attenuated in MAVS-KO mice may hint at a notion that ERVs are part of the antiviral immune defense. In humans, ERV activation was observed in different conditions, including HIV and cancer (53). In HIV, coexpression of ERV and HIV appears to inhibit HIV virion release (54). ERV expression in cancer cells may enhance antitumor immunity through activation of antiviral defense (55). Furthermore, cooptation of retrotransposon promoters to boost antiviral immunity is well documented (56). However, while immunologic ERV activation may have beneficial aspects in peripheral cells, it might be detrimental in the brain. Despite therapeutic advances against HIV, cognitive decline is common in long-term HIV survivors (54), showing an unmet clinical need. Even in the absence of HIV, aging and comorbidities associated with chronic inflammation may induce ERV activation in patients and contribute to cognitive decline.

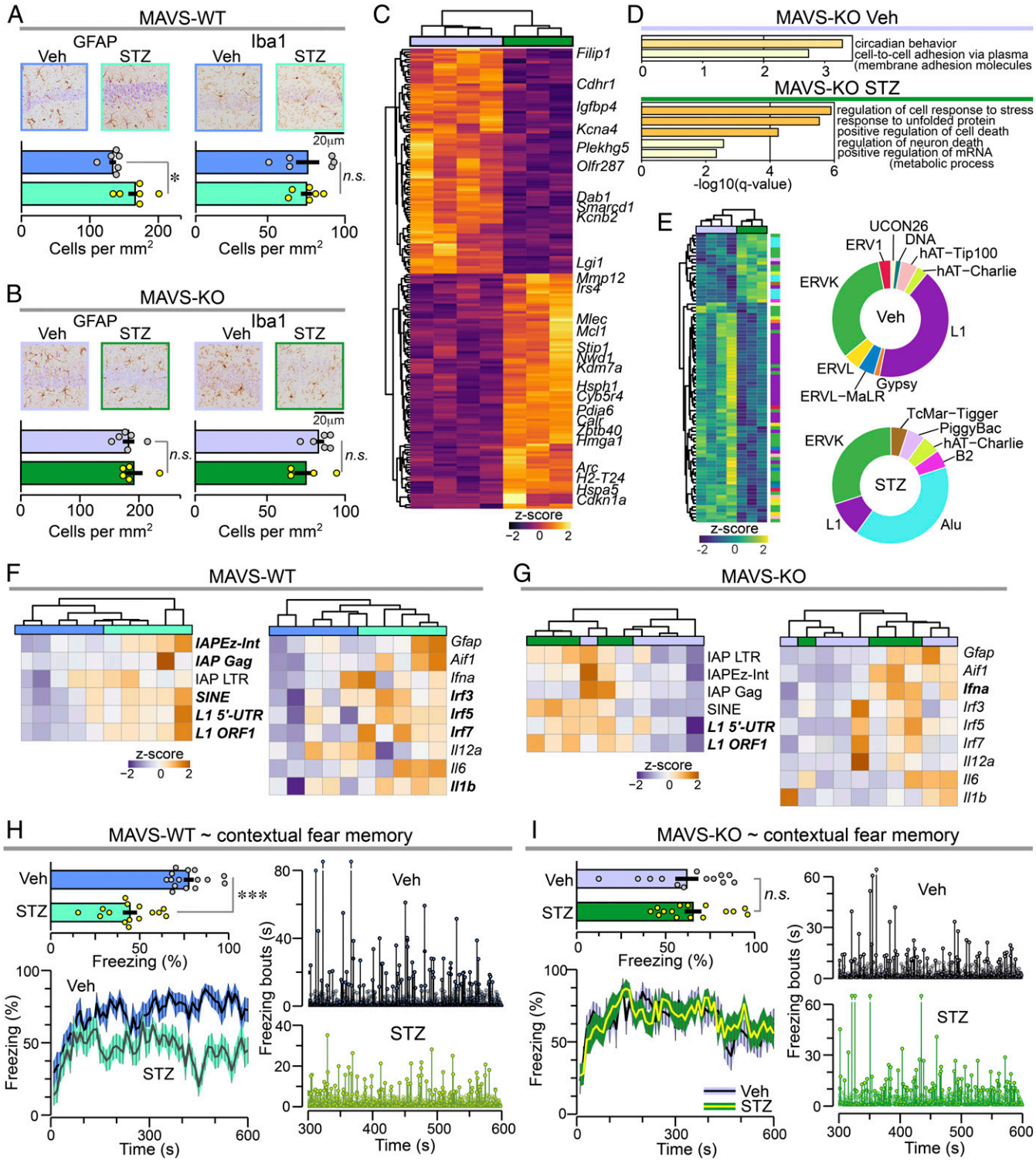

Fig. 5. MAVS-KO mice are resistant to ICVI-STZ–induced cognitive deficit. (*A* and *B*) Immunohistochemical cell density analysis of GFAP- and IBA1-positive cells in (*A*) MAVS-WT mice ($n = 6$ per group; $^*P < 0.05$, MWU test, 1 dot per mouse) and (*B*) MAVS-KO mice ($n = 5$ per group; *P* not significant [*n.s.*], MWU test; 1 dot per mouse). (*C*) Heatmap of differentially expressed genes obtained from RNA-seq of MAVS-KO mice ($n = 3$ ICVI-STZ, 94 genes; $n = 4$ ICVI-Veh, 90 genes). Selected genes are displayed next to the heatmap. (*D*) Selected enriched GO terms based on the differentially expressed genes from *C*. (*E*) Heatmap showing differentially expressed transposable elements (ICVI-STZ, 20 genes; ICVI-Veh, 64 genes) and donut plots depicting the composition of the differentially expressed transposable elements, color coded for the respective families. (*F* and *G*) Heatmaps of the qPCR results for selected retrotransposons (*Left*) and inflammation-related genes (*Right*) in MAVS-WT (*F*) and MAVS-KO (*G*) mice. Each cell represents 1 animal. Genes printed in bold type show statistical significance at $P < 0.05$. Note that hierarchical clustering separates ICVI-STZ and ICVI-Veh MAVS-WT mice with respect to retrotransposons and inflammation-related genes, while the expression of both gene groups is mixed in MAVS-KO mice. (*H* and *I*) Fear conditioning of MAVS-WT (*H*) and MAVS-KO (*I*) mice. (*Top Left*) bar graphs of the freezing response ($n = 15$ mice per group). $^{***}P < 0.001$ for MAVS-WT; $P = n.s.$ for MAVS-KO, MWU test; 1 dot per mouse. (*Bottom Left*) Freezing across the trial (mean ± SEM). (*Right*) Lollipop plots depicting durations of freezing bouts. Note the different heights of the *y*-axes with same scale for MAVS-WT mice but not MAVS-KO mice. The bar graphs in *A*, *B*, *H*, and *I* represent mean ± SEM.

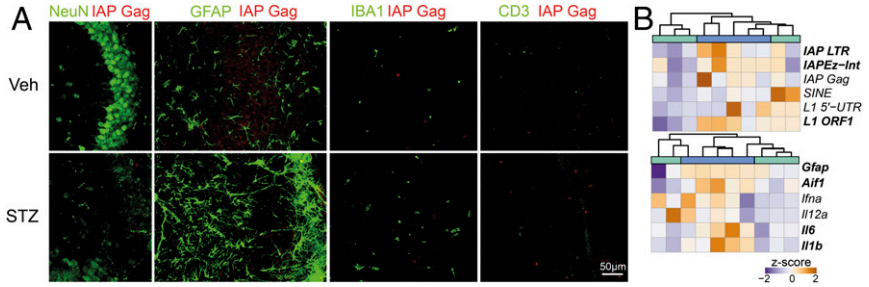

Fig. 6. STING deletion leads to pronounced gliosis and neurodegeneration after ICVI-STZ. (*A*) Immunohistochemistry of hippocampi of STING-KO mice treated with ICVI-STZ and ICVI-Veh, using NeuN, GFAP, IBA1, and CD3 costained with IAP Gag polyprotein. (*B*) Heatmaps of the qPCR results for selected retrotransposons (*Left*) and inflammation-related genes (*Right*). Each cell represents 1 animal. Genes printed in bold type show statistical significance at $P < 0.05$. Hierarchical clustering shows the separation of ICVI-STZ and ICVI-Veh.

It is important to note that ERV activation is only one of many features in both the muMT and ICVI-STZ models. muMT mice experience lifelong changes of the immune compartment that may affect brain development (43). STZ is a cytotoxin with broad effects on cell function. Thus, ERV sensing and antiviral immune response may be drivers of the cognitive deficit, but not necessarily other aspects of these models. There is a considerable body of literature using the ICVI-STZ model as a model of sporadic AD (41). While superficially, ICVI-STZ mice may exhibit some features similar to some hallmarks of human AD, fundamental differences in human and murine retrotransposon biology (12) make extrapolation of results between species quite challenging. Therefore, careful validation in human AD cases is essential in the interest of a common goal of finding causal AD treatments.

In conclusion, we have demonstrated that acute ERV activation in ICVI-STZ and chronic ERV activation in muMT mice are associated with impaired cognition in mice. Furthermore, our results point to MAVS as a molecular target for reducing retroviral element sensing. Our findings warrant the exploration of ERV as endogenous drivers of cognitive deficit in humans.

Materials and Methods

The protocols used in this study are fully described in the *SI Appendix, Materials and Methods*.

Animals. We used 5- to 8-mo-old male mice purchased from The Jackson Laboratory; mouse strains are listed in *SI Appendix*, Table S1. We performed all experiments in accordance with NIH guidelines, after approval by the Institutional Animal Care and Use Committee of the Feinstein Institutes for Medical Research, Northwell Health (Manhasset, NY).

Behavioral Testing. Animals were handled by the experimenter (3 consecutive days, 15 min per day) and then tested on the open field task to measure baseline anxiety and locomotion, the clockmaze test (57) to measure spatial learning, and the fear-conditioning test to measure fear learning and CFM. We used the software packages Ethovision XT11 (Noldus Information Technology) and FreezeFrame (Coulbourn Instruments) to track animals, organize the tests, and quantify behavioral data.

Intracerebroventricular Injections. Once anesthesia was achieved with isoflurane (3%), the head was restrained in a stereotaxic frame (David Kopf instruments). During aseptic surgery, vehicle (3 μL of citrate buffer, pH 4.5) or STZ solution (3 mg/kg) was administered stereotaxically (1.00 mm mediolateral, −0.3 mm anteroposterior, and −2.5 mm dorsoventral from bregma).

Ex Vivo Tissue Processing. Animals were euthanized using Euthasol and perfused with heparin NaCl solution. For immunohistochemistry, paraformaldehyde (4%) was also used for perfusion. For RNA extraction, the left hippocampus was homogenized in TRIzol (Thermo Fisher Scientific). For Western blot analysis, the left hippocampus was lysed in tissue protein extraction buffer with protease and phosphatase inhibitors (Thermo Fisher Scientific).

Brain Histology. The left hemisphere was fixed in paraformaldehyde (4%). Floating sections were prepared from 50-μm-thick sagittal slices. Formalin-fixed, paraffin-embedded tissues were sectioned into 3-μm sections and stained with antibodies (*SI Appendix*, Table S1). Antibody binding was visualized using horseradish peroxidase-conjugated secondary antibodies and Cresyl violet counterstaining. Coimmunostaining was performed using fluorescence-labeled secondary antibodies. Light transmission microscopy images were obtained and analyzed using the Leica Application Suite. Golgi staining was performed according to the manufacturer's instructions (FD Rapid GolgiStain Kit; FD NeuroTechnologies). Three-dimensional image stacks were traced using Neurolucida software (MBF Bioscience). Sholl analysis and morphological assessment of spine density were conducted using Neuroexplorer software (Nex Technologies). Statistical testing was conducted as described previously (58).

Cell Culture. Primary astrocytes were prepared from embryonic mouse brains on embryonic day 13.5 (*SI Appendix*, Table S1). LDH cell toxicity assays (Thermo Fisher Scientific) were performed according to the manufacturer's instructions.

Western Blot Analysis. Western blot analysis was performed using the Bio-Rad Western blotting system. Protein extracts (5 to 20 μg) from cell culture or brain lysates (50 to 100 μg) were used (*SI Appendix*, Table S1). Quantification was done using ImageJ.

qPCR and Bisulfite Sequencing. For qPCR, RNA (0.5 μg) was retrotranscribed using the iScript cDNA synthesis kit (Bio-Rad) and run on a LightCycler 480 PCR system (Roche Diagnostics). Targeted bisulfite sequencing was conducted as described previously (16, 21) using the EZ-DNA Methylation-Gold Kit (Zymo Research). The IAP Gag gene was amplified and subcloned using the pGEM-T Easy Vector System (Promega). Primers were chosen to recognize components of IAP and eMLV as described previously (16, 21). Expression of IAP-related elements coding for envelope (IAPE) retrotransposons was not specifically assessed in this study (59). Bisulfite sequencing analysis was performed using the Quantification Tool for Methylation Analysis (QUMA) web widget (60).

RNA-seq. Library preparation and RNA-seq for muMT and WT mice were performed at the service facility Centre of Excellence for Fluorescent Bioanalytics (www.kfb-regensburg.de). MAVS-WT and MAVS-KO mice were sequenced at the sequencing facility of the New York Genome Center. Paired-end sequencing was used for all experiments. Genome mapping of the fastq files was conducted using Star aligner using standard settings. FeatureCounts was used to generate gene count tables. Differential gene expression was analyzed using DESeq2 (61). Retrotransposon analysis of the RNA-seq data were conducted using TETools and DESeq2 following the publisher's instructions (62). GO term enrichment analysis was performed using Metascape (63). The raw data are available under the GEO accession no. GSE137782.

Statistical Analysis. Statistical analyses were performed using the R statistical programming environment (64) and Origin Pro software (Origin Lab). Parametric and nonparametric tests were chosen based on the underlying data structures. Adjustment for multiple testing was performed using the Benjamini–Hochberg method.

Data Availability. Our next-generation sequencing data are available at the Gene Expression Omnibus (accession no. GSE137782). The R code used to

prepare figures is provided at https://github.com/rsankowski/sankowski-et-al-pnas-2019/.

ACKNOWLEDGMENTS. We thank Bruce Volpe, Stefano Vergani, Reinhild Feuerstein, Kojie Horie, and Bryan Cullen for sharing reagents; Pedro Gomez, Eileen Barleon, and Tina El Gaz for excellent technical support; and Sonya VanPatten for suggestions and comments on the manuscript. R.S. was partly supported by a scholarship from the Hearst Foundation and the Berta-Ottenstein Programme for Clinician Scientists. P.T.H. was supported by NIH Grants 5P01AI102852 and 5P01AI073693.

1. E. S. Lander *et al.*; International Human Genome Sequencing Consortium, Initial sequencing and analysis of the human genome. *Nature* **409**, 860–921 (2001) Erratum in: *Nature* **411**, 720 (2001).
2. R. H. Waterston *et al.*; Mouse Genome Sequencing Consortium, Initial sequencing and comparative analysis of the mouse genome. *Nature* **420**, 520–562 (2002).
3. S. Carmi, G. M. Church, E. Y. Levanon, Large-scale DNA editing of retrotransposons accelerates mammalian genome evolution. *Nat. Commun.* **2**, 519 (2011).
4. N. Bannert, R. Kurth, The evolutionary dynamics of human endogenous retroviral families. *Annu. Rev. Genomics Hum. Genet.* **7**, 149–173 (2006).
5. C. Stocking, C. A. Kozak, Murine endogenous retroviruses. *Cell. Mol. Life Sci.* **65**, 3383–3398 (2008).
6. P. H. Sudmant *et al.*; 1000 Genomes Project Consortium, An integrated map of structural variation in 2,504 human genomes. *Nature* **526**, 75–81 (2015).
7. I. A. Maksakova *et al.*, Retroviral elements and their hosts: Insertional mutagenesis in the mouse germ line. *PLoS Genet.* **2**, e2 (2006).
8. M. Dewannieux, A. Dupressoir, F. Harper, G. Pierron, T. Heidmann, Identification of autonomous IAP LTR retrotransposons mobile in mammalian cells. *Nat. Genet.* **36**, 534–539 (2004).
9. J. A. Mietz, Z. Grossman, K. K. Lueders, E. L. Kuff, Nucleotide sequence of a complete mouse intracisternal A-particle genome: Relationship to known aspects of particle assembly and function. *J. Virol.* **61**, 3020–3029 (1987).
10. D. Ribet *et al.*, An infectious progenitor for the murine IAP retrotransposon: Emergence of an intracellular genetic parasite from an ancient retrovirus. *Genome Res.* **18**, 597–609 (2008).
11. D. B. Lombard *et al.*, DNA repair, genome stability, and aging. *Cell* **120**, 497–512 (2005).
12. J. H. Crichton, D. S. Dunican, M. Maclennan, R. R. Meehan, I. R. Adams, Defending the genome from the enemy within: Mechanisms of retrotransposon suppression in the mouse germline. *Cell. Mol. Life Sci.* **71**, 1581–1605 (2014).
13. F. Gaudet *et al.*, Induction of tumors in mice by genomic hypomethylation. *Science* **300**, 489–492 (2003).
14. G. Howard, R. Eiges, F. Gaudet, R. Jaenisch, A. Eden, Activation and transposition of endogenous retroviral elements in hypomethylation-induced tumors in mice. *Oncogene* **27**, 404–408 (2008).
15. K. B. Chiappinelli *et al.*, Inhibiting DNA methylation causes an interferon response in cancer via dsRNA including endogenous retroviruses. *Cell* **162**, 974–986 (2015). Erratum in: Cell **169**, 361 (2017).
16. D. S. Dunican *et al.*, Lsh regulates LTR retrotransposon repression independently of Dnmt3b function. *Genome Biol.* **14**, R146 (2013).
17. P. Yu *et al.*, Nucleic acid-sensing Toll-like receptors are essential for the control of endogenous retrovirus viremia and ERV-induced tumors. *Immunity* **37**, 867–879 (2012).
18. D. B. Stetson, J. S. Ko, T. Heidmann, R. Medzhitov, Trex1 prevents cell-intrinsic initiation of autoimmunity. *Cell* **134**, 587–598 (2008).
19. K. Kawane *et al.*, Chronic polyarthritis caused by mammalian DNA that escapes from degradation in macrophages. *Nature* **443**, 998–1002 (2006).
20. I. Triviai *et al.*, Endogenous retrovirus induces leukemia in a xenograft mouse model for primary myelofibrosis. *Proc. Natl. Acad. Sci. U.S.A.* **111**, 8595–8600 (2014).
21. G. R. Young *et al.*, Resurrection of endogenous retroviruses in antibody-deficient mice. *Nature* **491**, 774–778 (2012).
22. D. Gao *et al.*, Cyclic GMP-AMP synthase is an innate immune sensor of HIV and other retroviruses. *Science* **341**, 903–906 (2013).
23. C. H. Tie *et al.*, KAP1 regulates endogenous retroviruses in adult human cells and contributes to innate immune control. *EMBO Rep.* **19**, e45000 (2018).
24. R. Risser, J. M. Horowitz, J. McCubrey, Endogenous mouse leukemia viruses. *Annu. Rev. Genet.* **17**, 85–121 (1983).
25. B. K. Pal, S. Mohan, R. Nimo, M. B. Gardner, Wild mouse retrovirus-induced neurogenic paralysis in laboratory mice. I: Virus replication and expression in central nervous system. *Arch. Virol.* **77**, 239–247 (1983).
26. T. Odaka, Genetic transmission of endogenous N- and B-tropic murine leukemia viruses in low-leukemic strain C57BL/6. *J. Virol.* **15**, 332–337 (1975).
27. M. C. Appel, A. A. Rossini, R. M. Williams, A. A. Like, Viral studies in streptozotocin-induced pancreatic insulitis. *Diabetologia* **15**, 327–336 (1978).
28. A. A. Like, A. A. Rossini, Streptozotocin-induced pancreatic insulitis: New model of diabetes mellitus. *Science* **193**, 415–417 (1976).
29. E. H. Leiter, E. L. Kuff, Intracisternal type A particles in murine pancreatic B cells. Immunocytochemical demonstration of increased antigen (p73) in genetically diabetic mice. *Am. J. Pathol.* **114**, 46–55 (1984).
30. K. Mortelmans, F. Wang-Johanning, G. L. Johanning, The role of human endogenous retroviruses in brain development and function. *APMIS* **124**, 105–115 (2016).
31. R. K. Bhat *et al.*, Age- and disease-dependent HERV-W envelope allelic variation in brain: Association with neuroimmune gene expression. *PLoS One* **6**, e19176 (2011).
32. J. Feng *et al.*, Dnmt1 and Dnmt3a maintain DNA methylation and regulate synaptic function in adult forebrain neurons. *Nat. Neurosci.* **13**, 423–430 (2010).
33. W. Li *et al.*, Human endogenous retrovirus-K contributes to motor neuron disease. *Sci. Transl. Med.* **7**, 307ra153 (2015).
34. G. Arru *et al.*, Humoral immunity response to human endogenous retroviruses K/W differentiates between amyotrophic lateral sclerosis and other neurological diseases. *Eur. J. Neurol.* **25**, 1076–e84 (2018).
35. R. Douville, J. Liu, J. Rothstein, A. Nath, Identification of active loci of a human endogenous retrovirus in neurons of patients with amyotrophic lateral sclerosis. *Ann. Neurol.* **69**, 141–151 (2011).
36. M. Garcia-Montojo, W. Li, A. Nath, Technical considerations in detection of HERV-K in amyotrophic lateral sclerosis: Selection of controls and the perils of qPCR. *Acta Neuropathol. Commun.* **7**, 101 (2019).
37. J. M. Antony *et al.*, Human endogenous retrovirus glycoprotein-mediated induction of redox reactants causes oligodendrocyte death and demyelination. *Nat. Neurosci.* **7**, 1088–1095 (2004).
38. H. Perron *et al.*; The Collaborative Research Group on Multiple Sclerosis, Molecular identification of a novel retrovirus repeatedly isolated from patients with multiple sclerosis. *Proc. Natl. Acad. Sci. U.S.A.* **94**, 7583–7588 (1997).
39. C. Guo *et al.*, Tau activates transposable elements in Alzheimer's disease. *Cell Rep.* **23**, 2874–2880 (2018).
40. W. Li *et al.*, Activation of transposable elements during aging and neuronal decline in Drosophila. *Nat. Neurosci.* **16**, 529–531 (2013).
41. A. Nazem, R. Sankowski, M. Bacher, Y. Al-Abed, Rodent models of neuroinflammation for Alzheimer's disease. *J. Neuroinflammation* **12**, 74 (2015).
42. K. P. Doyle *et al.*, B-lymphocyte-mediated delayed cognitive impairment following stroke. *J. Neurosci.* **35**, 2133–2145 (2015).
43. S. Tanabe, T. Yamashita, B-1a lymphocytes promote oligodendrogenesis during brain development. *Nat. Neurosci.* **21**, 506–516 (2018).
44. T. J. Flanigan, Y. Xue, S. Kishan Rao, A. Dhanushkodi, M. P. McDonald, Abnormal vibrissa-related behavior and loss of barrel field inhibitory neurons in 5xFAD transgenics. *Genes Brain Behav.* **13**, 488–500 (2014).
45. J. A. Harris *et al.*, Many neuronal and behavioral impairments in transgenic mouse models of Alzheimer's disease are independent of caspase cleavage of the amyloid precursor protein. *J. Neurosci.* **30**, 372–381 (2010).
46. J. Kipnis, H. Cohen, M. Cardon, Y. Ziv, M. Schwartz, T cell deficiency leads to cognitive dysfunction: Implications for therapeutic vaccination for schizophrenia and other psychiatric conditions. *Proc. Natl. Acad. Sci. U.S.A.* **101**, 8180–8185 (2004).
47. Y. Chen *et al.*, Brain gene expression of a sporadic (icv-STZ mouse) and a familial mouse model (3xTg-AD mouse) of Alzheimer's disease. *PLoS One* **7**, e51432 (2012).
48. M. Murata, A. Takahashi, I. Saito, S. Kawanishi, Site-specific DNA methylation and apoptosis: Induction by diabetogenic streptozotocin. *Biochem. Pharmacol.* **57**, 881–887 (1999).
49. H. Ishikawa, G. N. Barber, STING is an endoplasmic reticulum adaptor that facilitates innate immune signalling. *Nature* **455**, 674–678 (2008).
50. R. B. Seth, L. Sun, C. K. Ea, Z. J. Chen, Identification and characterization of MAVS, a mitochondrial antiviral signaling protein that activates NF-kappaB and IRF 3. *Cell* **122**, 669–682 (2005).
51. S. Craft *et al.*, Intranasal insulin therapy for Alzheimer disease and amnestic mild cognitive impairment: A pilot clinical trial. *Arch. Neurol.* **69**, 29–38 (2012).
52. L. Lin, S. W. Yee, R. B. Kim, K. M. Giacomini, SLC transporters as therapeutic targets: Emerging opportunities. *Nat. Rev. Drug Discov.* **14**, 543–560 (2015).
53. K. Monde, R. Contreras-Galindo, M. H. Kaplan, D. M. Markovitz, A. Ono, Human endogenous retrovirus K Gag coassembles with HIV-1 Gag and reduces the release efficiency and infectivity of HIV-1. *J. Virol.* **86**, 11194–11208 (2012).
54. J. C. McArthur, HIV dementia: An evolving disease. *J. Neuroimmunol.* **157**, 3–10 (2004).
55. N. Bannert, H. Hofmann, A. Block, O. Hohn, HERVs new role in cancer: From accused perpetrators to cheerful protectors. *Front. Microbiol.* **9**, 178 (2018).
56. E. B. Chuong, N. C. Elde, C. Feschotte, Regulatory evolution of innate immunity through co-option of endogenous retroviruses. *Science* **351**, 1083–1087 (2016).
57. R. Sankowski *et al.*, Large-scale validation of the paddling pool task in the clockmaze for studying hippocampus-based spatial cognition in mice. *Front. Behav. Neurosci.* **13**, 121 (2019).
58. M. D. Wilson, S. Sethi, P. J. Lein, K. P. Keil, Valid statistical approaches for analyzing Sholl data: Mixed effects versus simple linear models. *J. Neurosci. Methods* **279**, 33–43 (2017).
59. F. U. Reuss, H. C. Schaller, cDNA sequence and genomic characterization of intracisternal A-particle-related retroviral elements containing an envelope gene. *J. Virol.* **65**, 5702–5709 (1991).
60. Y. Kumaki, M. Oda, M. Okano, QUMA: Quantification tool for methylation analysis. *Nucleic Acids Res.* **36**, W170–W175 (2008).
61. M. I. Love, W. Huber, S. Anders, Moderated estimation of fold change and dispersion for RNA-seq data with DESeq2. *Genome Biol.* **15**, 550 (2014).
62. E. Lerat, M. Fablet, L. Modolo, H. Lopez-Maestre, C. Vieira, TEtools facilitates big data expression analysis of transposable elements and reveals an antagonism between their activity and that of piRNA genes. *Nucleic Acids Res.* **45**, e17 (2017).
63. Y. Zhou *et al.*, Metascape provides a biologist-oriented resource for the analysis of systems-level datasets. *Nat. Commun.* **10**, 1523 (2019).
64. R Core Team, R: A language and environment for statistical computing (Version 3.6.1, R Foundation for Statistical Computing, Vienna, Austria, 2018. Available online at https://www.R-project.org.